Spectral-resolved cone-beam X-ray luminescence computed tomography with principle component analysis

HUANGSHENG PU, PENG GAO, JUNYAN RONG, WENLI ZHANG, TIANSHUAI LIU, AND HONGBING LU*

Department of Biomedical Engineering, Fourth Military Medical University, Xi'an, Shaanxi 710032, China
*luhb@fmmu.edu.cn

Abstract: Cone-beam X-ray luminescence computed tomography (CB-XLCT) has become a promising technique for its higher utilization of X-ray and shorter scanning time compared to the narrow-beam XLCT, but it suffers from the low-spatial resolution that results in the insufficiency to resolve the adjacent multiple probes. In multispectral CB-XLCT, multiple probes show different emission behaviors in the dimension of the spectrum. In this work, a spectral-resolved CB-XLCT method combining multispectral CB-XLCT with principle component analysis (PCA) was proposed to improve the imaging resolution. Results of digital simulation and the phantom experiment illustrated that the proposed method was capable of resolving adjacent multiple probes accurately and had better performance than the common multispectral CB-XLCT with spectrum information *priori*.

OCIS codes: (100.3010) Image reconstruction techniques; (100.3190) Inverse problems; (110.7440) X-ray imaging; (110.4234) Multispectral and hyperspectral imaging; (170.6280) Spectroscopy, fluorescence and luminescence; (170.3880) Medical and biological imaging.

References and links

1. G. Pratx, C. M. Carpenter, C. Sun, and L. Xing, "X-ray luminescence computed tomography via selective excitation: a feasibility study," IEEE Trans. Med. Imaging **29**(12), 1992–1999 (2010).
2. C. Li, K. Di, J. Bec, and S. R. Cherry, "X-ray luminescence optical tomography imaging: experimental studies," Opt. Lett. **38**(13), 2339–2341 (2013).
3. M. Ahmad, G. Pratx, M. Bazalova, and L. Xing, "X-ray luminescence and X-ray fluorescence computed tomography: new molecular imaging modalities," IEEE Access **2**(2), 1051–1061 (2014).
4. W. Cong and G. Wang, "X-ray fan-beam luminescence tomography," Austin J. Biomed. Eng. **1**(5), 1024 (2014).
5. D. Chen, S. Zhu, H. Yi, X. Zhang, D. Chen, J. Liang, and J. Tian, "Cone beam X-ray luminescence computed tomography: A feasibility study," Med. Phys. **40**(3), 031111 (2013).
6. X. Liu, Q. Liao, and H. Wang, "*In vivo* X-ray luminescence tomographic imaging with single-view data," Opt. Lett. **38**(22), 4530–4533 (2013).
7. X. Liu, Q. Liao, H. Wang, and Z. Yan, "Excitation-resolved cone-beam X-ray luminescence tomography," J. Biomed. Opt. **20**(7), 070501 (2015).
8. P. Gao, H. Pu, J. Rong, W. Zhang, T. Liu, W. Liu, Y. Zhang, and H. Lu, "Resolving adjacent nanophosphors of different concentrations by excitation-based cone-beam X-ray luminescence tomography," Biomed. Opt. Express **8**(9), 3952–3965 (2017).
9. A. D. Klose, "Hyperspectral excitation-resolved fluorescence tomography of quantum dots," Opt. Lett. **34**(16), 2477–2479 (2009).
10. A. J. Chaudhari, S. Ahn, R. Levenson, R. D. Badawi, S. R. Cherry, and R. M. Leahy, "Excitation spectroscopy in multispectral optical fluorescence tomography: methodology, feasibility and computer simulation studies," Phys. Med. Biol. **54**(15), 4687–4704 (2009).
11. A. D. Klose and T. Pöschinger, "Excitation-resolved fluorescence tomography with simplified spherical harmonics equations," Phys. Med. Biol. **56**(5), 1443–1469 (2011).
12. H. Pu, W. He, G. Zhang, B. Zhang, F. Liu, Y. Zhang, J. Luo, and J. Bai, "Separating structures of different fluorophore concentrations by principal component analysis on multispectral excitation-resolved fluorescence tomography images," Biomed. Opt. Express **4**(10), 1829–1845 (2013).
13. H. Pu, G. Zhang, W. He, F. Liu, H. Guang, Y. Zhang, J. Bai, and J. Luo, "Resolving fluorophores by unmixing multispectral fluorescence tomography with independent component analysis," Phys. Med. Biol. **59**(17), 5025–5042 (2014).

14. W. Cong, H. Shen, and G. Wang, "Spectrally resolving and scattering-compensated x-ray luminescence/fluorescence computed tomography," J. Biomed. Opt. **16**(6), 066014 (2011).
15. D. Chen, S. Zhu, X. Chen, T. Chao, X. Cao, F. Zhao, L. Huang, and J. Liang, "Quantitative cone beam X-ray luminescence tomography/X-ray computed tomography imaging," Appl. Phys. Lett. **105**(19), 191104 (2014).
16. H. Abdi and L. J. Williams, "Principal component analysis," WIREs Comp. Stat **2**(4), 433–459 (2010).
17. N. G. Anderson, A. P. Butler, N. J. A. Scott, N. J. Cook, J. S. Butzer, N. Schleich, M. Firsching, R. Grasset, N. de Ruiter, M. Campbell, and P. H. Butler, "Spectroscopic (multi-energy) CT distinguishes iodine and barium contrast material in MICE," Eur. Radiol. **20**(9), 2126–2134 (2010).
18. H. Gao, J. F. Cai, Z. Shen, and H. Zhao, "Robust principal component analysis-based four-dimensional computed tomography," Phys. Med. Biol. **56**(11), 3181–3198 (2011).
19. P. E. Svensson, J. Olsson, F. Engbrant, E. Bengtsson, and P. Razifar, "Characterization and reduction of noise in dynamic PET data using masked volumewise principal component analysis," J. Nucl. Med. Technol. **39**(1), 27–34 (2011).
20. P. Razifar, H. Engler, G. Blomquist, A. Ringheim, S. Estrada, B. Långström, and M. Bergström, "Principal component analysis with pre-normalization improves the signal-to-noise ratio and image quality in positron emission tomography studies of amyloid deposits in Alzheimer's disease," Phys. Med. Biol. **54**(11), 3595–3612 (2009).
21. E. Eyal, B. N. Bloch, N. M. Rofsky, E. Furman-Haran, E. M. Genega, R. E. Lenkinski, and H. Degani, "Principal component analysis of dynamic contrast enhanced MRI in human prostate cancer," Invest. Radiol. **45**(4), 174–181 (2010).
22. E. M. C. Hillman and A. Moore, "All-optical anatomical co-registration for molecular imaging of small animals using dynamic contrast," Nat. Photonics **1**(9), 526–530 (2007).
23. X. Liu, D. Wang, F. Liu, and J. Bai, "Principal component analysis of dynamic fluorescence diffuse optical tomography images," Opt. Express **18**(6), 6300–6314 (2010).
24. M. Schweiger, S. R. Arridge, M. Hiraoka, and D. T. Delpy, "The finite element method for the propagation of light in scattering media: Boundary and source conditions," Med. Phys. **22**(11), 1779–1792 (1995).
25. P. C. Hansen, "Analysis of discrete ill-posed problems by means of the L-curve," SIAM Rev. **34**(4), 561–580 (1992).
26. J. Feng, K. Jia, G. Yan, S. Zhu, C. Qin, Y. Lv, and J. Tian, "An optimal permissible source region strategy for multispectral bioluminescence tomography," Opt. Express **16**(20), 15640–15654 (2008).
27. R. Lansford, G. Bearman, and S. E. Fraser, "Resolution of multiple green fluorescent protein color variants and dyes using two-photon microscopy and imaging spectroscopy," J. Biomed. Opt. **6**(3), 311–318 (2001).
28. J. Yang, Z. Quan, D. Kong, X. Liu, and J. Lin, "Y_2O_3:Eu^{3+} microspheres: solvothermal synthesis and luminescence properties," Cryst. Growth Des. **7**(4), 730–735 (2007).
29. R. Michels, F. Foschum, and A. Kienle, "Optical properties of fat emulsions," Opt. Express **16**(8), 5907–5925 (2008).
30. L. R. Dice, "Measures of the amount of ecologic association between species," Ecology **26**(3), 297–302 (1945).
31. L. Zhang, F. Gao, H. He, and H. Zhao, "Three-dimensional scheme for time-domain fluorescence molecular tomography based on Laplace transforms with noise-robust factors," Opt. Express **16**(10), 7214–7223 (2008).
32. X. Liu, B. Zhang, J. Luo, and J. Bai, "Principal component analysis of dynamic fluorescence tomography in measurement space," Phys. Med. Biol. **57**(9), 2727–2742 (2012).
33. P. R. Peres-Neto, D. A. Jackson, and K. M. Somers, "How many principal components? stopping rules for determining the number of non-trivial axes revisited," Comput. Stat. Data Anal. **49**(4), 974–997 (2005).
34. C. Li, G. S. Mitchell, J. Dutta, S. Ahn, R. M. Leahy, and S. R. Cherry, "A three-dimensional multispectral fluorescence optical tomography imaging system for small animals based on a conical mirror design," Opt. Express **17**(9), 7571–7585 (2009).
35. W. Zhang, Y. Shen, M. Liu, P. Gao, H. Pu, L. Fan, R. Jiang, Z. Liu, F. Shi, and H. Lu, "Sub-10 nm water-dispersible β-$NaGdF_4$:X% Eu^{3+} nanoparticles with enhanced biocompatibility for *in vivo* X-ray luminescence computed tomography," ACS Appl. Mater. Interfaces **9**(46), 39985–39993 (2017).

1. Introduction

The feasibility of X-ray luminescence computed tomography (XLCT) was first demonstrated by Xing's group in narrow-beam X-ray mode [1]. The principle of XLCT is that the nanoparticles can emit visible or near-infrared (NIR) luminescence when excited by X-ray beams and then the distribution of nanoparticles can be reconstructed from the projection data of luminescence [2,3]. Compared to the regular optical molecular tomography, the main advantages of XLCT are the increased excitation depth in tissue and the elimination of tissue autofluorescence.

The narrow-beam XLCT showed good spatial resolution, but it suffered from the long scanning time which hindered its practical application to some extent. For fast imaging, different excitation modes of X-ray were studied. Cong *et al.* used fan-beam X-ray to excite nanoparticles in XLCT and can reduce scanning time, but it still need slice-by–slice scanning

[4]. The cone-beam XLCT (CB-XLCT) was first proposed by Chen *et al*. [5], and applied to small animal experiment by Liu *et al*. [6]. Compared to the narrow-beam and fan-beam mode, CB-XLCT can illuminate the whole body and stimulate all the nanoparticles simultaneously, so it can improve the X-ray utilization and reduce the scanning time greatly which is critical for clinical application. However, CB-XLCT suffered from the ill-posed reconstruction which resulted in low-spatial resolution, and the ill-posed problem became worse for *in vivo* imaging due to the high scattering characteristic of photons in biological tissue. As a result, it is a challenge for CB-XLCT to resolve multiple probes especially when they are adjacent.

Efforts have been done to resolve the multiple probes in CB-XLCT recently. Multi-voltage excitation scheme were used to resolve multiple targets of different kinds by Liu *et al*. [7] and of different concentrations in our previous work in CB-XLCT [8]. Compared to multi-voltage excitation scheme, multispectral scheme could be another optional choice. Multispectral scheme has been applied in optical molecular tomography successfully [9–13], and were taken into account in XLCT recently [14,15]. Cong *et al*. validated the feasibility of multispectral scheme in pencil-beam XLCT by the numerical mouse simulation [14]. Chen *et al*. used spectrum information as *priori* to improve the reconstruction quality for single probe in CB-XLCT [15]. Though some efforts have been devoted to multispectral XLCT, no studies about multispectral scheme have been reported for resolving multiple probes in CB-XLCT to our knowledge.

Compared with conventional CB-XLCT, multispectral CB-XLCT cannot only obtain more valid luminescence data but also get the different emission information of the multiple probes in the dimension of spectrum. An exposition of resolving multiple probes can come down to an analysis of the correlative data obtained over spectrums, so multivariate analysis can be applied to multispectral CB-XLCT for the purpose. As a popular multivariate statistical technique, principal component analysis (PCA) can be used to extract spatial information from the original data by computing principal components (PCs) which are linear combinations of the original data [16]. PCA has been widely used in various imaging technologies, such as computed tomography (CT) [17,18], positron emission tomography (PET) [19,20] and magnetic resonance imaging (MRI) [21]. In optical molecular imaging, PCA was used to analyze optical data varying with times [22,23], spectrums [12] and energies [7,8]. Despite of these successful applications of PCA, no trials have been reported to use PCA in multispectral CB-XLCT. As PCA is a data-driven method and CB-XLCT has its own characteristics of poor spatial resolution, investigation on the application of PCA in multispectral CB-XLCT is very important.

In this work, a new method called spectral-resolved CB-XLCT by combining multispectral CB-XLCT with PCA was proposed to resolve adjacent multiple probes. Digital simulation and phantom experiments were performed to test the performance of the proposed method, and multispectral CB-XLCT with spectrum information *priori* was also studied for comparison. The qualitative and quantitative evaluations suggest that the method of performing PCA on multispectral CB-XLCT images is capable of resolving adjacent multiple probes accurately.

The outline of this paper is as follows. In Section 2, the basic theories of multispectral CB-XLCT with spectrum information *priori* and the proposed spectral-resolved CB-XLCT are detailed. In Section 3, the methods of experiments and evaluations are described. The results are illustrated and evaluated in Section 4. Finally, we discuss and conclude the major findings of this work.

2. Theories

2.1 Forward model

In CB-XLCT, the light propagation mainly contains two parts: propagations of the X-ray to the nanoparticles and the emission light from nanoparticles [5]. Based on Lambert-Beer law,

during the propagation course of X-ray through the tissues, the X-ray intensity $\chi(\mathbf{r})$ along the primary path can be expressed as:

$$\chi(\mathbf{r}) = \chi(\mathbf{r}_0) \exp\{-\int_{r_0}^{r} \mu_x(\tau)\,\mathrm{d}\tau\} \tag{1}$$

where $\chi(\mathbf{r}_0)$ is the X-ray source intensity at the initial position $\mathbf{r}_0$, and μ_x is the X-ray attenuation coefficient which can be obtained from XCT. The emission light source $S(r_s)$ excited by X-ray at position r_s can be described as follows:

$$S(r_s) = \chi(r_s)\eta\rho(r_s) \tag{2}$$

where ρ is the nanoparticle concentration and χ is the X-ray intensity. η is the light yield which is the intrinsic property of the nanoparticle and can be experimentally determined. Light yield is defined as the total quantum yield at all emission wavelengths per unit nanoparticle concentration and X-ray intensity usually.

The emission light transported in the tissues can be expressed by the diffusion equation (DE) approximately [5]:

$$\nabla[D(r)\nabla\Phi(r)] - \mu_a(r)\Phi(r) = -S(r_s) \tag{3}$$

where $D(r)$ is the diffusion coefficient, Φ is the photon density and μ_a is the absorption coefficient. By discretizing the reconstruction region to N voxels, the above imaging model can be converted into the following linear relationship based on the finite-element method (FEM) [24]:

$$\mathbf{W}x = \Phi_m \tag{4}$$

where x is the unknown N×1 column vector for reconstruction which is proportional to nanoparticle concentration distribution ρ with the relationship of $x = \rho\,\eta$ and the weighted matrix $\mathbf{W}$ describes the forward model from the unknown vector x to the known measurements Φ_m.

The emission photons at all wavelengths are taken into account to define η in conventional CB-XLCT with no optical filters, and η can be taken as constant for a certain nanoparticle. But in multispectral CB-XLCT, η should be taken as variable. And Eq. (4) can be rewritten as follows:

$$\mathbf{W}(\lambda_k)x(\lambda_k) = \Phi_m(\lambda_k) \tag{5}$$

where $x(\lambda_k) = \rho\,\eta(\lambda_k)$ is the unknown column vector for reconstruction and $\eta(\lambda_k)$ is the light yield of the corresponding nanoparticle at each wavelength λ_k. Traditional Tikhonov regularization method was used to solve the inverse problem in Eqs. (4) and (5) [25].

2.2 Multispectral CB-XLCT with spectrum information

In the common multispectral CB-XLCT, the spectral information (SI) about $\eta(\lambda_k)$ are usually used as a *priori* information. Light yield should be taken as variable denoted as $\eta(\lambda_k) = \omega(\lambda_k)\eta$, where $\omega(\lambda_k)$ is the relative fraction at the corresponding wavelength λ_k to the total emission luminescence spectrum. For nanoparticle of a certain kind, the relative fraction $\omega(\lambda_k)$ can be determined by performing a spectral analysis in advance, where

$\omega(\lambda_k) \geq 0$ and $\sum \omega(\lambda_k) \approx 1$. Thus, the *priori* information can be used directly and Eq. (5) can be redefined by the following matrix model [15, 26]:

$$\begin{bmatrix} \mathbf{W}(\lambda_1)\eta(\lambda_1) \\ \mathbf{W}(\lambda_2)\eta(\lambda_2) \\ \vdots \\ \mathbf{W}(\lambda_k)\eta(\lambda_k) \end{bmatrix} \boldsymbol{\rho} = \begin{bmatrix} \Phi_m(\lambda_1) \\ \Phi_m(\lambda_2) \\ \vdots \\ \Phi_m(\lambda_k) \end{bmatrix} \tag{6}$$

But for multiple nanoparticles of different kinds, the Eq. (6) is not applicable. The position information *priori* of multiple nanoparticles are not available in common cases, so light yields cannot be assigned to each kind nanoparticle correspondingly at each wavelength. The reconstruction targets $x(\lambda_k)$ in the Eq. (5) are the combination of multiple nanoparticles, so $x(\lambda_k)$ at wavelength λ_k can be expressed as the following:

$$x(\lambda_k) = \boldsymbol{\rho}_1 \eta_1(\lambda_k) + \boldsymbol{\rho}_2 \eta_2(\lambda_k) \cdots + \boldsymbol{\rho}_P \eta_P(\lambda_k) \tag{7}$$

where P is the number of nanoparticle kinds and $\boldsymbol{\rho}_P$ is distribution of the P-th kind nanoparticle. Then $x(\lambda_k)$ for all wavelengths can be denoted as:

$$[\boldsymbol{\rho}_1 \quad \boldsymbol{\rho}_2 \quad \cdots \quad \boldsymbol{\rho}_P] \mathbf{A} = [x(\lambda_1) \quad x(\lambda_2) \quad \cdots \quad x(\lambda_M)] \tag{8}$$

where $\mathbf{A} = \begin{bmatrix} \eta_1(\lambda_1) & \eta_1(\lambda_2) & \cdots & \eta_1(\lambda_M) \\ \eta_2(\lambda_1) & \eta_2(\lambda_2) & \cdots & \eta_2(\lambda_M) \\ \vdots & \vdots & \vdots & \vdots \\ \eta_P(\lambda_1) & \eta_P(\lambda_2) & \cdots & \eta_P(\lambda_M) \end{bmatrix}$..

To get $\boldsymbol{\rho}_P$ from Eq. (8), it is critical that number of wavelengths M should satisfy the condition $M \geq P$. In the work, the number of wavelengths taken into account was set to be equal to P for simplification. $\mathbf{A}$ can be obtained by spectral analysis experiments as spectrum information *priori*, and then the distribution of each kind nanoparticle can be recovered from Eq. (8).

2.3 Multispectral CB-XLCT with PCA

Another way to obtain the individual distributions of multiple nanoparticles from $x(\lambda_k)$ data is using an unmixing technique [27]. Multivariate analysis such as PCA can be used for the purpose. The reconstructed results in multispectral CB-XLCT were assembled as the input matrix for PCA, which can be denoted as $\mathbf{X} = \{x(\lambda_1), ..., x(\lambda_k), ..., x(\lambda_M)\}$. $\mathbf{X}$ is normalized to the maximal value in this work. After PCA, a $N \times M$ matrix $\mathbf{P}$ of the principle components (PCs) can be obtained as follows [12]:

$$\mathbf{P} = \mathbf{X_0} \mathbf{E} \tag{9}$$

where $\mathbf{X_0}$ is the centered data of $\mathbf{X}$ by subtracting its column means and the j-th principle component which is the j-th column of $\mathbf{P}$ can be denoted as:

$$p_j = \mathbf{X_0} e_j \tag{10}$$

where e_j is the j-th column vector of $\mathbf{E}$. The absolute values of positive and negative elements in PCs are further utilized to create images respectively, from which the spatial distribution of multiple nanoparticles can be obtained. The function (*princomp*) in MATLAB software (MathWorks, Natick, MA, USA) was used to perform PCA in this work. The

methods of conventional CB-XLCT with no optical filters, the multispectral CB-XLCT with spectrum information *priori* and the multispectral CB-XLCT with PCA are denoted hereafter as C-NF, M-SI and M-PCA methods, respectively.

3. Methods

3.1 Digital simulation

The model for digital simulation was composed of a cylinder containing two spheres, as shown in Fig. 1. The radius of the cylinder was 1.5 cm and the height was 3.0 cm. Probes A and B with the same radius of 0.2 cm were placed at the same height of Z = 1.5 cm and have an edge-to-edge distance (EED) of 0.2 cm. The cylinder was supposed to be filled with 1% intralipid solution with homogenous optical properties. The concentrations of probes A and B were set to 2 mg/ml and 2.5 mg/ml, respectively. The total quantum yields of two probes were set same for simplification. The relative fractions of probes A and B at four different spectral bands which have the center wavelengths of 580 nm, 620nm, 660 nm and 700 nm with about 40 nm full width at half maximum (FWHM) were set as Table 1.
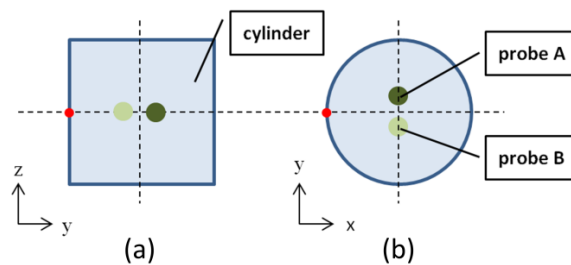

Fig. 1. Illustration of cylinder model. (a) The coronal view. (b) The transverse view.

Table 1. The relative fraction $\omega(\lambda_k)$ in digital simulation

	580 nm	620 nm	660 nm	700 nm
probe A	0.30	0.50	0.10	0.06
probe B	0.40	0.20	0.15	0.05

The simulation model was rotated for 360°, with 12 projections acquired from the cylinder surface with an angular increment of 30°. Then, zero-mean white Gaussian noise was added to simulate the real noisy boundary measurements with signal-to-noise ratio (SNR) set as 35 dB.

3.2 Phantom experiment

A custom-made multispectral CB-XLCT system developed by our laboratory was adopted in the phantom experiments for validation. As shown in Fig. 2(a), the CB-XLCT system consists of a micro-focus X-ray source (Oxford Instrument, U.K.) with the maximal power of 80 W, a highly sensitive electron-multiplying CCD (EMCCD) camera (iXon DU-897, Andor, U.K.), which is coupled with a 50 mm f/1.8D lens (Nikon, Melville, N.Y.) for luminescence data acquisition, and a CMOS X-ray detector (2923, Dexela, U.K.) for the transmitted X-ray collection. EMCCD is placed in a 4 mm thickness lead box for protecting it from X-ray irradiation. The optical filter (Rayan Technology, China) in front of the EMCCD is used to choose the pass band in multispectral CB-XLCT.
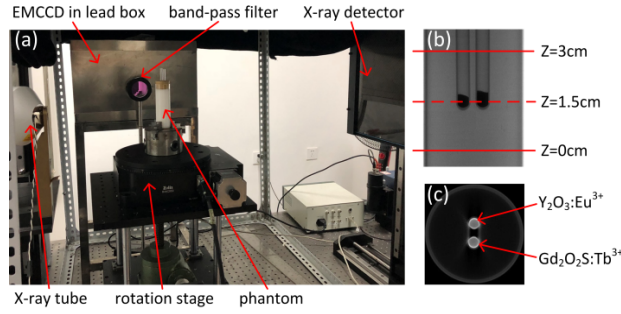
Fig. 2. Illustrations of imaging system and phantom. (a) Multispectral CB-XLCT system. (b) X-ray projection of the phantom and the reconstruction region is between two red solid lines. (c) XCT slice of the phantom, corresponding to Z = 1.5 cm in (b).

As shown in Fig. 2(b), a transparent glass cylinder (outer diameter 3.0 cm) embedded two glass tubes (outer diameter 0.4 cm) with an EED about 0.22 cm was used for the phantom experiments. The glass cylinder was filled with 1% intralipid solution diluted by water to mimic biological tissue. As shown in Fig. 2(c), the glass tubes filled with different nanoparticle powders $Y_2O_3{:}Eu^{3+}$ and $Gd_2O_2S{:}Tb^{3+}$ were used as multiple probes. $Y_2O_3{:}Eu^{3+}$ and $Gd_2O_2S{:}Tb^{3+}$ have several obvious emission peaks with the maximum at the wavelengths of 610 nm and 545 nm respectively [15,28]. Two band-pass optical filters which have the center wavelengths of 580 nm and 620 nm with about 40 nm FWHM were used for luminescence data collection in multispectral CB-XLCT. The region for reconstruction is about 3 cm height and the corresponding optical parameters were set at each wavelength [29].

To keep the total number of projections same as that in conventional CB-XLCT with no optical filters, the number of projections in multispectral CB-XLCT was reduced to 12 at each spectral band for two spectral bands are studied. The luminescence data were acquired at 24 projections with 15° step in the conventional CB-XLCT with no optical filters, and at 12 projections with 30° step in the multispectral CB-XLCT. During the luminescence data collection, the X-ray tube voltage and current were set to 40 kVp and 1 mA, respectively. The integration time, EM gain and binning of EMCCD were set to 1 s, 260 and 1 × 1, respectively.

3.3 Evaluation

To evaluate the spatial similarity between the actual regions and the computed regions, the Dice coefficient is calculated as [30]:

$$\text{Dice} = \frac{2|X \cap Y|}{|X| + |Y|} \quad (11)$$

where $|\cdot|$ denotes the number of voxels. X describes actual regions and Y describes the computed regions which are obtained by M-SI or M-PCA methods. The bigger value of Dice coefficient stands for the higher spatial similarity and the max value is 1.

The location error (LE) is used to evaluate the localization accuracy of the proposed methods. It is given by calculating the Euclidean distance between centroids of the actual and computed regions:

$$\text{LE} = \left\| \boldsymbol{p}_a - \boldsymbol{p}_c \right\|_2 \quad (12)$$

where $\boldsymbol{p}_a$ and $\boldsymbol{p}_c$ denote the centroids of the actual and computed regions which are obtained by M-SI or M-PCA methods, respectively.

In order to further quantitatively analyze the performance of the proposed methods in resolving the two targets, a relative coefficient is defined as [31]:

$$R = \frac{u_{max} - u_{valley}}{u_{max} - u_{min}} \tag{13}$$

where u denote the values of the profile along a given line. u_{max} and u_{min} are the maximal and minimal values of u, respectively. u_{valley} denotes the valley value between the two peak values corresponding to two targets. According to the definition, the value of R denotes the spatial resolution, where R = 1 represents the highest spatial resolution and R = 0 represents the lowest spatial resolution.

4. Results

4.1 Digital simulation

4.1.1 Images reconstructed at different spectral bands
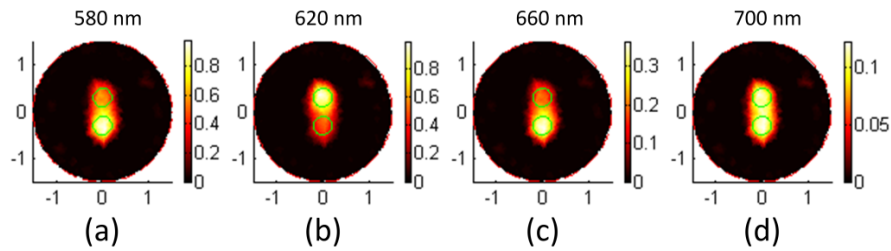
Fig. 3. Reconstruction results at different spectral bands with center wavelengths of (a) 580 nm, (b) 620 nm, (c) 660 nm and (d) 700 nm.

The reconstruction results at different spectral bands are illustrated in Fig. 3. As shown in Fig. 3, two probes A and B are mixed together, and it is difficult to resolve them from these reconstructed tomographic images at each single spectral band. The height of the displayed reconstruction slice is 1.5 cm. The actual boundaries of two probes are located by two small green circles.

4.1.2 The results of M-SI method

The results of traditional M-SI method are illustrated in Fig. 4. As shown in Fig. 4, the distributions of probes A and B can be recovered by M-SI method, respectively. The M-SI method is based on the first two spectral bands with center wavelengths of 580 nm and 620 nm.
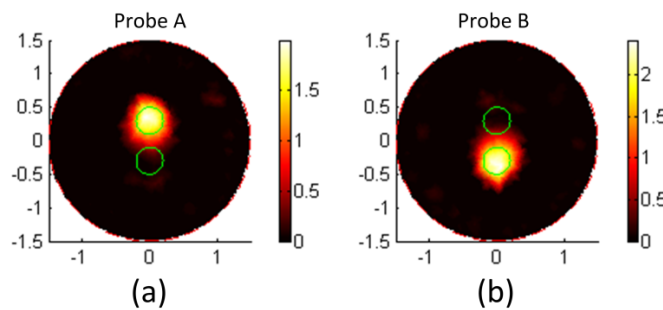

Fig. 4. Results of M-SI method in digital simulation. Distributions of (a) probe A and (b) probe B recovered by M-SI method.

4.1.3 Application of M-PCA on different combinations of multi-spectral data

Different combinations of spectral bands were used to test the performance of M-PCA method. As shown in Table 2, four spectral bands with center wavelengths of 580 nm, 620

nm, 660 nm and 700 nm were used as case 1, three spectral bands with center wavelengths of 580 nm, 620 nm and 660 nm were used as case 2, and two spectral bands with center wavelengths of 580 nm and 620 nm were used as case 3.

Table 2. Different combinations of multiple spectral bands

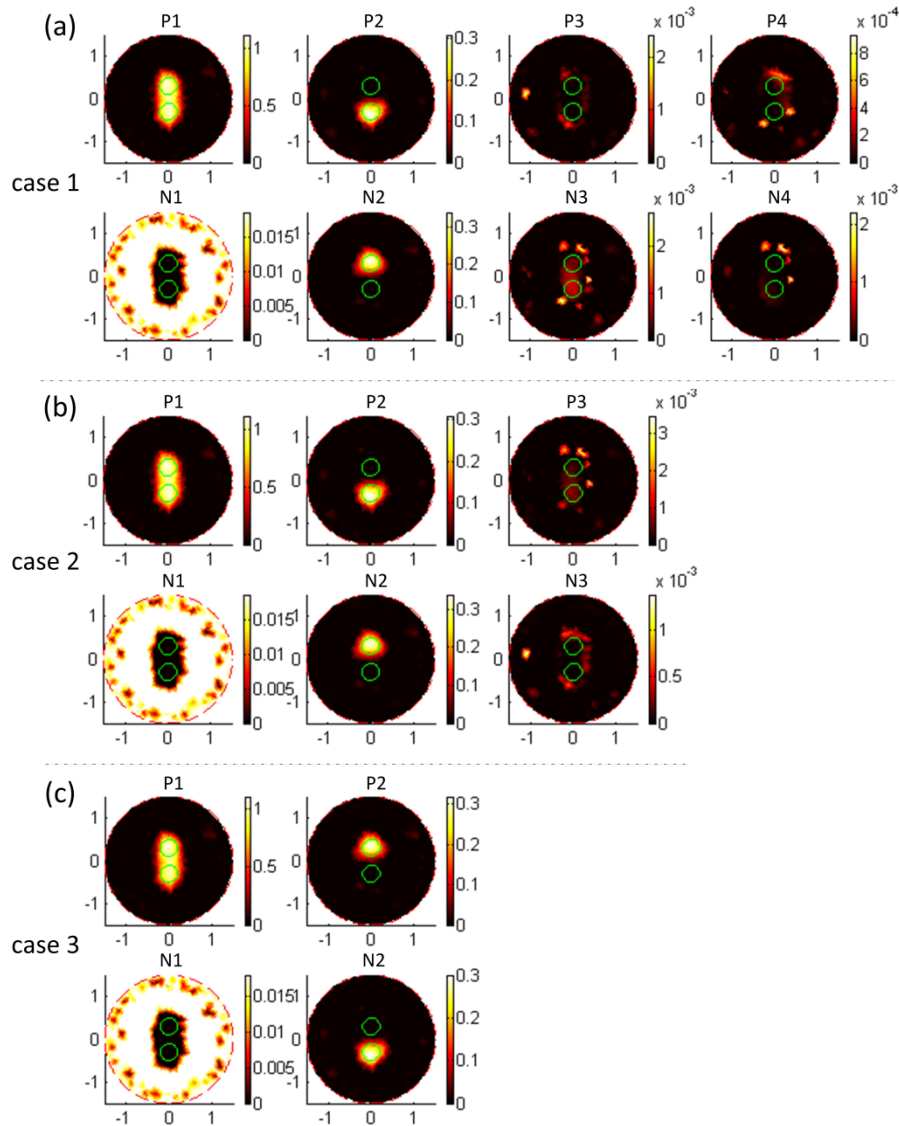| case #	spectral band combination (nm)	number of spectral bands
case 1	580,620,660,700	4
case 2	580,620,660	3
case 3	580,620	2

Fig. 5. The obtained PCs by M-PCA method in (a) case 1, (b) case 2 and (c) case 3. For each case, the images in the first row are the positive PCs, and the images in the second row are the negative PCs.

PCs obtained by M-PCA method of case 1, case 2 and case 3 are shown in Fig. 5. For each case, the images in the first row are the positive PCs, and the images in the second row

are the negative PCs. In case 1, as shown in Fig. 5(a), the probes A and B are resolved by N2 image and P2 image, which were the negative and positive elements of PC2, respectively. Higher-order components, PC3 and PC4, contained less structure information of targets and their intensities were much smaller than that of PC2. In case 2, as shown in Fig. 5(b), the probes A and B are also well resolved by N2 image and P2 image, respectively. Similarly, the higher-order component, PC3, kept less information of target signals. As shown in Fig. 5(c), the probes A and B are resolved by P2 image and N2 image in case 3, respectively.

The transformation course from centered original data X_0 to the obtained P is described in Eq. (9). While transforming X_0 to P, the total variance keeps the same value which means that PCA does not change the total energy. In this work, the cumulated percentages of variances were calculated [32]. The percentages of variance (eigenvalue) in each PC and cumulated percentages of the first several PCs are displayed in Table 3. As shown in Table 3, the first two PCs account for most of the total variance for all cases.

Table 3. The percentage and cumulated percentages of variances in PCs (%)

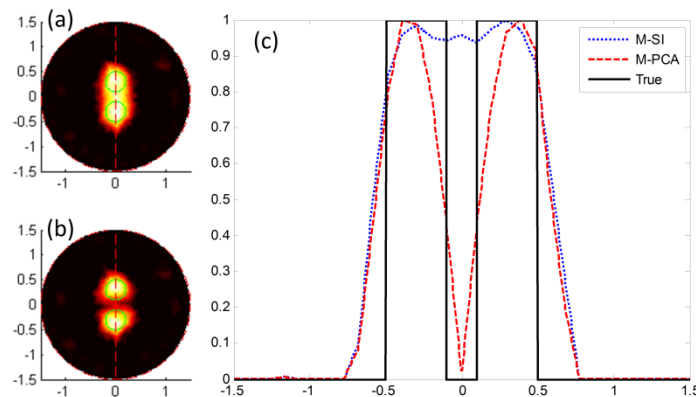|	case 1		case 2		case 3	
PCs	percentage	cumulated percentage	percentage	cumulated percentage	percentage	cumulated percentage
PC1	92.4866	92.4866	92.4055	92.4055	92.4858	92.4858
PC2	7.5124	99.9990	7.5940	99.9995	7.5142	100.0000
PC3	0.0008	99.9998	0.0005	100.0000		
PC4	0.0002	100.0000				

4.1.4 Evaluation

Fig. 6. Merged images of probes obtained by (a) M-SI method and (b) M-PCA method in case 3. (c) Intensity profiles along the red dash lines in (a) and (b).

As shown in Fig. 6, the images of two probes are merged in the same image in order to evaluate the spatial resolution. Figure 6(a) is the merged results of probes A and B recovered by M-SI method illustrated in Figs. 4(a) and 4(b). Figure 6(b) is the merged results of PC2 images by M-PCA method in case 3 illustrated in Fig. 5(c). All images are normalized to their maximal intensive value before mergence for comparison. The profiles across the two probes along the red dash lines (Y-axis) in Figs. 6(a) and 6(b) are shown in Fig. 6(c) in order to better clarify the spatial resolution. The FWHM of the profiles obtained with M-SI is larger than that of M-PCA and the valley value between the two peaks obtained with M-SI is much larger than that of M-PCA. To quantitatively analyze the spatial resolution, the index R defined in Eq. (13) for each profile in Fig. 6(c) is listed in Table 4. As shown in Table 4, R value is 0.9750 by M-PCA method in case 3 and 0.0639 by M-SI method, which illustrated that the M-PCA method can obtain much higher spatial resolution than M-SI method.

The performances of M-SI and M-PCA methods for all cases are further evaluated quantitatively with Dice, LE, and R indexes, as shown in Table 4. The merged PC2 images obtained by M-PCA and the merged image by M-SI were used to compute these indexes and LE was the mean value of LEs of both probes. Compared with M-SI, higher Dice values indicated that M-PCA reserved the target shape better, lower average LE indicated that the positions of the two probes determined by M-PCA method was closer to their actual positions, and higher R indicated that M-PCA obtained much higher spatial resolution. In addition, the proposed M-PCA method exhibited similar performances for all cases, especially those for case 1 and case 2. It indicates that the proposed M-PCA method could resolve two targets with only two spectral bands, which was validated qualitatively by Fig. 6 and quantitatively by Table 4.

Table 4. The quantitative evaluation of M-PCA and M-SI in digital simulation

	M-SI	M-PCA(case1)	M-PCA(case2)	M-PCA(case3)
Dice	0.6667	0.7987	0.7987	0.7995
LE (mm)	0.3866	0.2061	0.2062	0.2109
R	0.0639	0.9569	0.9571	0.9750

4.2 Phantom experiment

4.2.1 Reconstructions of C-NF with different projections

The reconstruction images of C-NF method with different projections are shown in Fig. 7. It is difficult to resolve the adjacent multiple probes from these reconstructed images even with 24 projections in C-NF method. The qualities of the reconstruction images become worse with the number of projections decreasing.
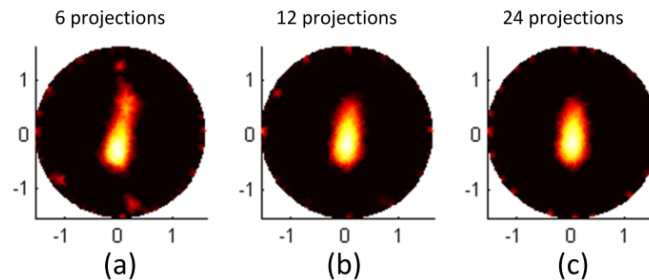

Fig. 7. Reconstruction results of C-NF with (a) 6 projections, (b) 12 projections and (c) 24 projections. The height of the reconstruction slices is 1.5 cm.

4.2.2 The results of the M-SI method

In order to get the spectrum information *priors* for M-SI method, a spectral analysis were performed in advance. The emitted photons from nanoparticles $Y_2O_3:Eu^{3+}$ and $Gd_2O_2S:Tb^{3+}$ at the wavelengths from 400 nm to 800 nm with an interval of 1 nm were measured by spectrometer. Then $\eta(\lambda_k)$ of the pass bands of optical filters and thus the relative fractions $\omega(\lambda_k)$ of the band pass optical filters with center wavelengths of 580 nm and 620 nm can be calculated and are shown in Table 5.

Table 5. The relative fraction $\omega(\lambda_k)$ in phantom experiment

	580 nm	620 nm
$Y_2O_3:Eu^{3+}$	0.27	0.56
$Gd_2O_2S:Tb^{3+}$	0.13	0.08

The reconstruction results at spectral bands with the center wavelengths of 580 nm and 620 nm are shown in Figs. 8(a) and 8(b), respectively. It is hard to resolve the multiple probes from the reconstruction results. The reconstruction values are normalized by the maximum value of both spectral bands. As shown in Figs. 8(c) and 8(d), the distributions of nanoparticles $Y_2O_3:Eu^{3+}$ and $Gd_2O_2S:Tb^{3+}$ can be obtained by M-SI method, respectively.
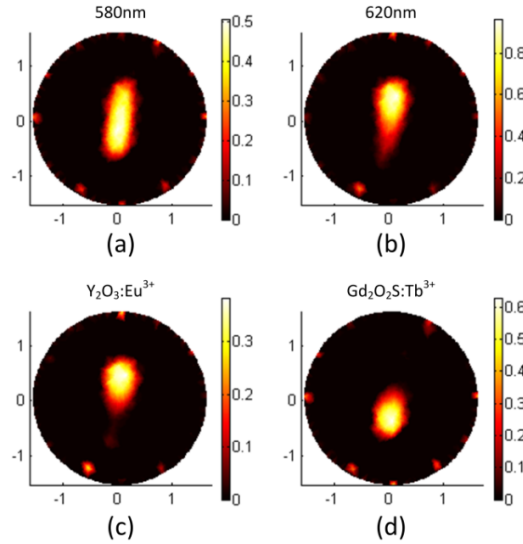

Fig. 8. Results of reconstruction and M-SI method in phantom experiment. (a) and (b) Reconstruction results at 580 nm and 620 nm. (c) and (d) Distributions of nanoparticles $Y_2O_3:Eu^{3+}$ and $Gd_2O_2S:Tb^{3+}$ obtained by M-SI method.

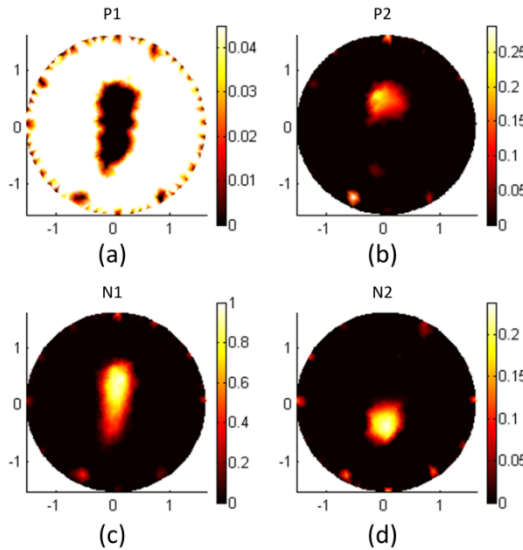### 4.2.3 The results of the M-PCA method

Fig. 9. Results of M-PCA method in phantom experiment. (a) and (b) The positive elements in the first and second PCs. (c) and (d) The negative elements in the first and second PCs.

The PCs obtained by M-PCA method are shown in Fig. 9. The images in the first row and in the second row are the positive and negative PCs. The nanoparticle powder $Y_2O_3:Eu^{3+}$ and $Gd_2O_2S:Tb^{3+}$ in the glass tubes on behalf of multiple probes are illustrated by the positive and

negative elements in PC2 respectively, as shown in P2 image in Fig. 9(b) and N2 image in Fig. 9(d).

4.2.4 Evaluation

The performance of C–NF, M-SI and M-PCA methods are compared in Fig. 10 qualitatively. The reconstruction images of C–NF method with 24 projections are shown in the first row. The merged results of Figs. 8(c) and 8(d) by M-SI method with 12 projections are shown in the second row. The PC2 images (the merged results of P2 and N2 images in Fig. 9) by M-PCA method with 12 projections are shown in the third row. The first column images are the fusion image of CB-XLCT and XCT images. The second and third column images are different views of 3D renderings. The comparison illustrated that M-SI and M-PCA methods can resolve the adjacent probes rather than C–NF, and the performance of M-PCA is better than M-SI.

The performance of M-SI and M-PCA methods are further evaluated quantitatively with Dice, LE and R indexes. LE is the mean value of LEs of $Y_2O_3:Eu^{3+}$ and $Gd_2O_2S:Tb^{3+}$. R value is calculated using the values along the red dash line (Y-axis) as shown in Figs. 10(d) and 10(g), respectively. As shown in Table 6, M-PCA method has the higher Dice coefficient, smaller LE value and much larger R coefficient than M-SI method. These indexes quantitatively confirm M-PCA has better performance on resolving multiple probes than M-SI as shown in Fig. 10.
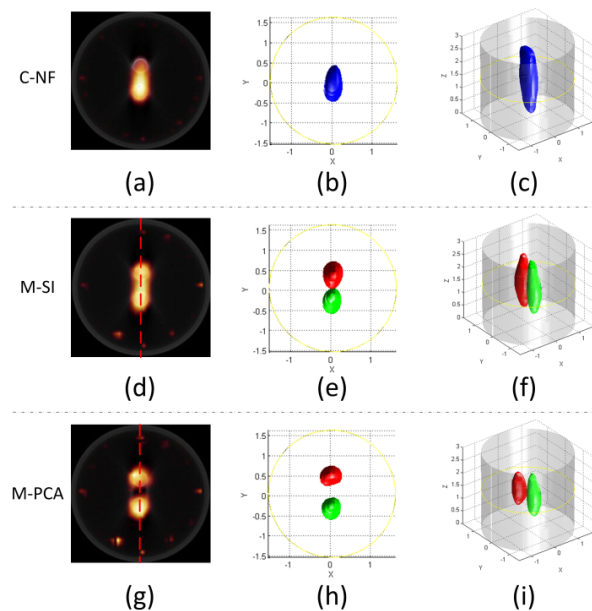

Fig. 10. Qualitative comparisons of C–NF, M-SI and M-PCA methods. (a), (d) and (g) Fusion images of C–NF, M-SI and M-PCA with the corresponding XCT slice respectively. (b) and (c) Different views of 3D rendering of C–NF. (e) and (f) Different views of 3D rendering of M-SI. (h) and (i) Different views of 3D rendering of M-PCA.

Table 6. The quantitative evaluation of M-SI and M-PCA in phantom experiment

	M-SI	M-PCA
Dice	0.7246	0.8324
LE (mm)	0.5033	0.3215
R	0.1547	0.9760

5. Discussion and conclusion

CB-XLCT has got development for its higher utilization of X-ray and shorter scanning time compared to the narrow-beam XLCT, but it suffers from the low-spatial resolution due to the ill-posed optical reconstruction. So it is hard to resolve the multiple reconstruction targets especially when they are adjacent in conventional CB-XLCT with no optical filters. In this work, a spectral-resolved CB-XLCT method which combined multispectral CB-XLCT with PCA was proposed for multiple probe imaging, and the performance was evaluated by digital simulation and phantom experiment further.

Two probes with EED of 0.2 cm in digital simulation and two tubes with EED about 0.22 cm in phantom experiments were used as the adjacent multiple targets. As shown in the reconstruction images, the two targets cannot be separated through C-NF (Fig. 7) or CB-XLCT with single spectral band (Figs. 3, 8(a) and 8(b)). Meanwhile it is difficult to recognize the structure of the targets. But two targets can be resolved both by M-SI (Figs. 4, 8(c) and 8(d)) and M-PCA (Figs. 5, 9(b) and 9(d)) methods. Compared to M-SI method, the proposed M-PCA method has better performance on resolving adjacent multiple targets, which can be validated by the merged images (Figs. 6 and 10) qualitatively and the evaluation indexes (Tables 4 and 6) quantitatively. In addition, the performances of the proposed M-PCA method are tested with different combinations of spectral bands in digital simulations. The similar performance in case 3 to that in other cases indicated that two targets can be resolved by the proposed M-PCA method with only two spectral bands which was further validated by the phantom experiments in this work.

According to the principle of PCA, the recovered signals generally appeared in the first several components which has been testified in the previous studies [7,8,12,22,23]. How many principal components should be chosen can be determined to many rules [33]. In this work, the cumulated percentages of variances were calculated to choose the proper principal components which have been validated in optical imaging modalities [32]. For the resolving of two targets, most information of target signals is kept in the second PC, as shown in previous studies [7, 8, 12]. In this study, two targets with different behaviors were successfully resolved in PC2, too. But for the cases of low signal to noise ratio (SNR), two targets may appear in the higher-order PCs, such as in PC3 [23], so more PCs may needs to be considered for those special cases. In addition, more PCs should be considered if there are three or more targets, and combination of several components may be work in the cases for which single component is incapable.

Clearly with the multispectral detection, just as multi-voltage excitation, the proposed method would increase the imaging time and thus the radiation dose compared to the conventional CB-XLCT. In the phantom experiments, the projections at each spectral band were reduced to 12 in order to keep the total projection numbers same as that in the conventional CB-XLCT with no optical filters. Another purpose for this is to eliminate the effects of the increasing amount of the detection data on the performance of the proposed method. In addition, as described in our previous work in which two voltage excitations were used, radiation dose measured for 48 projections are still acceptable for *in vivo* imaging [8]. Several schemes could be taken to decrease the radiation dose further. Firstly, the total number of projections should be as small as possible. On one hand, fewer spectral bands should be used. In this work, experimental results indicated that two adjacent probes could be accurately resolved by the proposed method with only two spectral bands. On the other hand, the projections at each spectral band in multispectral CB-XLCT should be limited. But with the decreased projections, the reconstruction quality became worse just as shown in Fig. 7. The reconstruction method with limited projections can be considered [6]. Secondly, using the mirror design to collect projections of different angles simultaneously in the multispectral CB-XLCT as that in other optical imaging method may increase the time efficiency and decrease the X-ray dose [34].

Compared to other optical imaging modalities such as fluorescence molecular tomography (FMT) and bioluminescence tomography (BLT), XLCT is newly developed and its advance depends greatly on the development of X-ray excitable luminescent nanoparticles (XLNP). Currently, the synthesis of water-soluble and bio-compatible XLNPs is still a challenge for most groups working on XLCT, resulting in few *in vivo* XLCT studies reported so far. Our group has put great effort on the synthesis of XLNPs and successfully prepared a water-dispersible β-NaGdF$_4$:15% Eu^{3+} nanoparticles in the end of last year [35]. However, in the present work, different types of soluble XLNP were needed to exhibit different excitation spectra, which have not been available yet. Therefore, different kinds of nanoparticle powders instead of solutions were used to test the feasibility of the proposed method. With the development of water-dispersible XLNPs, it is expected that XLCT imaging would advance greatly by phantom experiments, *in vitro* and *in vivo* small animal studies with XLNP solutions.

In conclusion, the proposed method which combined multispectral CB-XLCT with PCA provides an attractive approach for imaging multiple probes according to the results of digital simulation and phantom experiment. For multiple probes, the emission luminescence shows different variation trends with spectrum. Since PCA can catch emission behaviors of different varying trends, the M-PCA method can be applied to resolve targets filled with different nanoparticles. It would not work for targets containing the same nanoparticle with different concentrations because they have the same varying trend. If the linear assumption is not satisfied or the emission spectrum changes with concentrations, more research is needed. The independent component analysis could be considered further in multispectral CB-XLCT to get the concentration information.

Funding

Disclosures

The authors declare that there are no conflicts of interest related to this article.